



## Full length article

## A natural energy absorbent polymer composite: The equine hoof wall

Wei Huang<sup>a</sup>, Nicholas A. Yaraghi<sup>b</sup>, Wen Yang<sup>a</sup>, Alexis Velazquez-Olivera<sup>c</sup>, Zezhou Li<sup>a</sup>, Robert O. Ritchie<sup>d</sup>, David Kisailus<sup>b,e</sup>, Susan M. Stover<sup>f</sup>, Joanna McKittrick<sup>a,c,\*</sup>

<sup>a</sup> Materials Science and Engineering Program, University of California San Diego, La Jolla, CA, United States

<sup>b</sup> Materials Science and Engineering Program, University of California Riverside, Riverside, CA, United States

<sup>c</sup> Department of Mechanical and Aerospace Engineering, University of California San Diego, La Jolla, CA, United States

<sup>d</sup> Department of Materials Science and Engineering, University of California Berkeley, Berkeley, CA, United States

<sup>e</sup> Department of Chemical and Environmental Engineering, University of California Riverside, Riverside, CA, United States

<sup>f</sup> School of Veterinary Medicine, University of California Davis, Davis, CA, United States

## ARTICLE INFO

## Article history:

Received 9 November 2018

Received in revised form 26 March 2019

Accepted 1 April 2019

Available online 3 April 2019

## Keywords:

Equine hoof

Keratin

Energy absorption

Tubular structure

Mechanical properties

## ABSTRACT

The equine hoof has been considered as an efficient energy absorption layer that protects the skeletal elements from impact when galloping. In the present study, the hierarchical structure of a fresh equine hoof wall and the energy absorption mechanisms are investigated. Tubules are found embedded in the inter-tubular matrix forming the hoof wall at the microscale. Both tubules and intertubular areas consist of keratin cells, in which keratin crystalline intermediate filaments (IFs) and amorphous keratin fill the cytoskeletons. Cell sizes, shapes and IF fractions are different between tubular and intertubular regions. The structural differences between tubular and intertubular areas are correlated to the mechanical behavior of this material tested in dry, fresh and fully hydrated conditions. The stiffness and hardness in the tubule areas are higher than that in the intertubular areas in the dry and fresh samples when loaded along the hoof wall; however, once the samples are fully hydrated, the intertubular areas become stiffer than the tubular areas due to higher water absorption in these regions. The compression behavior of hoof in different loading speed and directions are also examined, with the isotropy and strain-rate dependence of mechanical properties documented. In the hoof walls, mechanistically the tubules serve as a reinforcement, which act to support the entire wall and prevent catastrophic failure under compression and impact loading. Elastic buckling and cracking of the tubules are observed after compression along the hoof wall, and no shear-banding or severe cracks are found in the intertubular areas even after 60% compression, indicating the highly efficient energy absorption properties, without failure, of the hoof wall structure.

## Statement of Significance

The equine hoof wall is found to be an efficient energy absorbent natural polymer composite. Previous studies showed the microstructure and mechanical properties of the hoof wall in some perspective. However, the hierarchical structure of equine hoof wall from nano- to macro-scale as well as the energy absorption mechanisms at different strain rates and loading orientations remains unclear. The current study provides a thorough characterization of the hierarchical structure as well as the correlation between structure and mechanical behaviors. Energy dissipation mechanisms are also identified. The findings in the current research could provide inspirations on the designs of impact resistant and energy absorbent materials.

© 2019 Acta Materialia Inc. Published by Elsevier Ltd. All rights reserved.

\* Corresponding author at: Department of Mechanical and Aerospace Engineering, University of California San Diego, La Jolla, CA, United States.

E-mail address: [jmckittrick@ucsd.edu](mailto:jmckittrick@ucsd.edu) (J. McKittrick).

## 1. Introduction

Keratin is one of the most common natural structural biopolymers (protein-based) with remarkable mechanical properties that generate different functionalities in natural materials, such as in offensive weapons in sheep horns, defensive armor in pangolin

scales and turtle shells, protective and energy absorptive layers in animal hooves and as environmental barriers in bird feathers and animal hairs [1–4]. Indeed, energy absorption is one of the most important properties of keratin in tissues under extreme loadings [5]. Although solely composed of polymer constituents, keratin is one of the toughest natural materials. The toughness of keratin is greater than bone and wood, which are considered structural biological materials with light weight and high fracture toughness [6,7]. Bighorn sheep fight with each other, reaching speeds of  $\sim 9$  m/s with a deceleration of  $\sim 450$  g, which creates large amounts of impact energy [8,9]. The peak force during the fighting between bighorn sheep normalized by their body weight can reach 34 N/kg, which is comparable with the force generated in a car collision at a speed of 30 mph ( $\sim 33$  N/kg) [10]. An unshod horse trotting at  $\sim 4$  m/s on an asphalt surface has a deceleration  $\sim 56$  g, resulting a peak ground reacting force  $\sim 11.5$ – $16.1$  N/kg [11]. The deceleration depends on the ground surfaces upon which hooves are landing: on dirt and turf surfaces, hooves have deceleration  $\sim 43$  g, while synthetic surfaces only result in  $\sim 28.5$  g [12]. The vertical landing velocity of the hoof increases slightly with an increasing speed, indicating a slightly higher ground reaction force and deceleration at a higher running speed [13]. Although sustaining less impact than horns, the high frequency of the contact with the surfaces also requires excellent energy absorption properties [14,15]. Thus, it is of interest to understand the mechanical properties and fundamental energy absorption mechanisms of these keratinous materials.

Keratin is produced in epithelial cells, having a composite structure in which crystalline intermediate filaments (IFs) are embedded in an amorphous matrix [16–18]. The IFs are classified into two categories based on the molecular arrangements:  $\alpha$ -helix and  $\beta$ -sheet.  $\alpha$ -keratin is mainly found in mammals while  $\beta$ -keratin is found in avian and reptilian tissues [1,19]. The hierarchical structures of keratin with different morphologies, such as hair and wool, beaks, claws, scales, fingernails, horns and hooves, are well documented [20–25]. At the nanoscale level, these materials are composed of the crystalline IFs ( $\sim 7$ – $10$  nm), which consist of coiled-coil keratin dimer sub-units within an amorphous matrix containing mostly keratin-associated proteins that have a high sulfur content [26–28]. These further form macrofibrils (diameter  $\sim 100$ – $400$  nm) in disk-shaped cells (diameter  $\sim 20$ – $30$   $\mu\text{m}$ ). The differences of the nanostructures between different keratins are the percentage and orientation of the IFs (22%–31% in equine hoof,  $\sim 46\%$  in human hair,  $\sim 56\%$  in wool,  $\sim 100\%$  in hagfish slime threads) [29–31]. At the microscale level, the cells stack layer-by-layer (layer thickness  $\sim 2$   $\mu\text{m}$ ) to form a lamellar structure. Additionally, both horns and hooves have micrometer-sized tubules embedded in the lamellae while the other examples do not [23,32]. In both hooves and horns, the tubules have continuous medullary cavities, however the tubular structure is more complicated in hooves [32,33]. The hoof material results from epithelial proliferation on the coronary papillae, which further form the tubular areas and ‘flat’ regions of dermis between the papillae, and evolve into the intertubular areas [32,34]. In the bighorn sheep horns, no tubular areas were identified, but only medullary cavities compose the tubules [8,23]. It has been shown that the tubules in bighorn sheep horn play important roles in terms of impact resistance and energy absorption [23,35]. Tubule closure and microbuckling were identified as the primary energy absorption mechanisms that protect bighorn sheep heads from high-speed impacts [8]. Though both contain tubules, the tubules in hooves exhibit a different structure from those found in horns including cell arrangements, tubular densities and IF orientations [8,36]. Accordingly, it is of interest to study the energy absorption capabilities of the hoof wall as a comparison to the previous studies on the bighorn sheep horns [8] to understand the different structural

designs evolved by nature to identify potential designs for impact resistant bioinspired materials.

Kasapi and Gosline [36] examined the design complexities of the equine hoof wall structure, and found that tubule sizes and shape, densities, IF arrangements were dependent on the location throughout the thickness direction of the hoof wall. Cells in the tubules were found to be almost perpendicular to the cell planes in the intertubular matrix in which the cell planes are almost parallel with the ground surface. These authors conducted tensile and fracture toughness tests to study the mechanical behavior of the hoof wall [30,36]; they concluded that the different orientations of the IFs in the tubules and intertubular matrix served to effectively redirect crack propagation, thereby increasing the toughness. Tensile properties of the tubules and matrix, acquired by micro-tensile testing at a strain rate  $\sim 3.3 \times 10^{-3} \text{ s}^{-1}$ , showed that the stiffness was not uniform, being  $\sim 0.29$  GPa in the tubular area and  $\sim 0.14$  GPa in the intertubular matrix at the center of hoof wall. The strain rate was similar to the previous tensile tests performed on horns and hairs [23,30,35]. The yield strength in these two areas, however, was similar;  $\sim 4.8$  MPa in the tubules and  $\sim 4.1$  MPa in the intertubular matrix. It was concluded that the orientations of the IFs and their volume fractions ( $\sim 23\%$  in tubules,  $\sim 30\%$  in intertubular areas) were the main factors affecting the mechanical properties [30,37]. Douglas *et al.* [38] reported that the tensile and compressive stiffnesses were higher at the distal region than that at the proximal region of the hoof wall at both medial and lateral sites, which may provide stress protection to the inner living tissues. Hydration effects on the mechanical properties have also been investigated [39]; these studies revealed a significant decrease in tensile modulus in the dry versus fully hydrated samples. The tensile properties of the hoof wall were also found to be strain-rate sensitive [40], both tensile stiffness and strength increasing with increasing strain rate.

In this study, we present a more detailed structural characterization of the hoof wall using high-resolution characterization with synchrotron x-ray micro-computed tomography and transmission electron microscopy, coupled with extensive mechanical property evaluation. With regards to the latter, compression tests were conducted in different orientations and at different strain rates to evaluate the energy absorption properties. Additionally, modulus and hardness mapping were performed using nanoindentation to acquire the local mechanical properties of tubule and intertubular matrix areas. *In situ* synchrotron x-ray computed tomography compression tests were conducted to analyze the energy absorption mechanisms of the hoof. The main goals of the current study were to characterize the hierarchical structure-mechanical property relationships in hoof wall keratin to fully define the energy absorption mechanisms during compressive loading. We believe that our findings will provide inspiration for future bioinspired designs of energy-absorbent synthetic structures and materials.

## 2. Experiments and methods

### 2.1. Micro- and nanoscale structural characterization

Fresh horse hooves were acquired from the School of Veterinary Medicine, University of California Davis. A convenience sample of 3 unilateral forelimb hooves from 3 adult Thoroughbred horses was obtained postmortem from horses that died for reasons unrelated to hoof pathology. The horses were  $\sim 5$  years old and had an average weight  $\sim 450$ – $500$  kg. The hooves were stored in  $-20$  °C and kept frozen before testing. Hoof samples with three different hydration states were prepared for experiments in this study: ambient dry ( $\sim 8.8$  wt%  $\text{H}_2\text{O}$ ), fresh ( $\sim 30.2$  wt%  $\text{H}_2\text{O}$ ) and fully hydrated ( $\sim 40$  wt%  $\text{H}_2\text{O}$ ). The water contents were measured by

using the methods described previously [8]. In brief, the weight changes of fresh samples were measured before and after drying in an oven at 130 °C for 24 h. Fully hydrated samples were acquired by immersing the samples in deionized (DI) water for three days until there was no increase in the weight. The water content of fresh and fully hydrated samples in the current study were found to be similar to previous work (~27.9 wt%–35.5 wt% in fresh hooves, ~40.2 wt% in fully hydrated samples) [38].

Fig. 1a and b show an intact equine hoof and its mid-sagittal section, with the bone tissue and keratinized hoof wall marked. A higher magnification image with an additional transverse section is shown in Fig. 1c, indicating where the samples were extracted. Three directions are defined: the longitudinal direction is proximal to distal; the radial direction is axial to abaxial; the transverse direction is orthogonal to the two other directions. Three samples, with dimension  $2 \times 2 \times 2$  mm, were acquired from the central part of the hoof wall. Due to the similar mechanical behavior observed from outer to inner positions of the hoof wall based on the previous literatures [30,36], the current study focused on the middle part of the hoof wall as a representative sampling area. A representative location of the samples was indicated in Fig. 1c (orange box). Samples were thawed at room temperature prior to synchrotron x-ray computed microtomography (XCT) imaging. Three other samples with the same dimension were fixed with 2.5% glutaraldehyde solution for 24 hrs. After washing with DI water three times, 2% osmium tetroxide ( $\text{OsO}_4$ ) was used to stain the samples for three days to increase the contrast; the samples were then finally washed with DI water five times. Both stained and unstained samples were scanned with XCT, which was performed on the tomography beamline 8.3.2 at the Advanced Light Source (Lawrence Berkeley National Laboratory, Berkeley, USA), using an x-ray accelerating voltage of 25 keV, with a field of view of  $1.7 \times 1.7$  mm at a resolution of  $0.65 \mu\text{m}$  per voxel. 1025 radiographs were collected during a given scan over a rotation of  $180^\circ$ . The series of .tiff images were reconstructed using the Amira software (FEI Visualization

Sciences Group, Burlington, MA, USA) with a module of volume rendering.

Samples (six in total, two samples from each hoof) were cut into  $4 \times 4 \times 4$  mm<sup>3</sup> cubes for further optical and electron microscopy characterization. The locations of the samples were the same as the samples prepared in the XCT tests to keep consistent. Flat surfaces of the longitudinal and transverse sections were prepared by an ultramicrotome (Leica EM UC6, Leica Microsystems Inc., Buffalo Grove, IL, USA) for optical microscopy (OM) studies. Differential interference contrast (DIC) OM images were taken on the prepared flat surfaces using a Keyence VHX 1000 microscope (Keyence, Palatine, IL, USA). Toluidine blue stained thin slices ( $\sim 1 \mu\text{m}$  thick, 6 slices from each cube) were prepared by an ultramicrotome and imaged to examine cell shapes, sizes and distribution. The dimensions and distributions of medulla cavities and tubules were measured from the OM images in three different sites (Fig. S1). Three cubes were fixed with a 2.5 vol% glutaraldehyde solution overnight, and subsequently dehydrated in a graded series of ethanol solutions (20%, 40%, 60%, 80%, 95%, and 100% vol.% ethanol). These samples were then freeze-fractured in liquid nitrogen for examination by scanning electron microscopy (SEM); they were sputter coated with iridium (Quorum Technologies Ltd., West Sussex, UK) to enhance the sample electron conductivity. SEM imaging was conducted with an ultra-high-resolution microscope (FEI, Hillsboro, OR, USA). The three remaining cubes were stained with 2%  $\text{OsO}_4$  solution for three days for transmission electron microscopy (TEM) imaging. The stained samples were washed with DI water five times followed by the dehydration process mentioned previously. The samples were then embedded in Spurr's low viscosity resin (Electron Microscopy Sciences, Hatfield, PA, USA) and cut into  $\sim 80$  nm thin sections using an ultramicrotome (Leica EM UC6, Leica Microsystems Inc., Buffalo Grove, IL, USA). The sections were placed on copper grids, post-stained using lead citrate solutions to enhance contrast, and imaged with a FEI Tecnai 12 (Spirit) (80 kV) transmission electron microscope (FEI, Hillsboro, Oregon, USA).

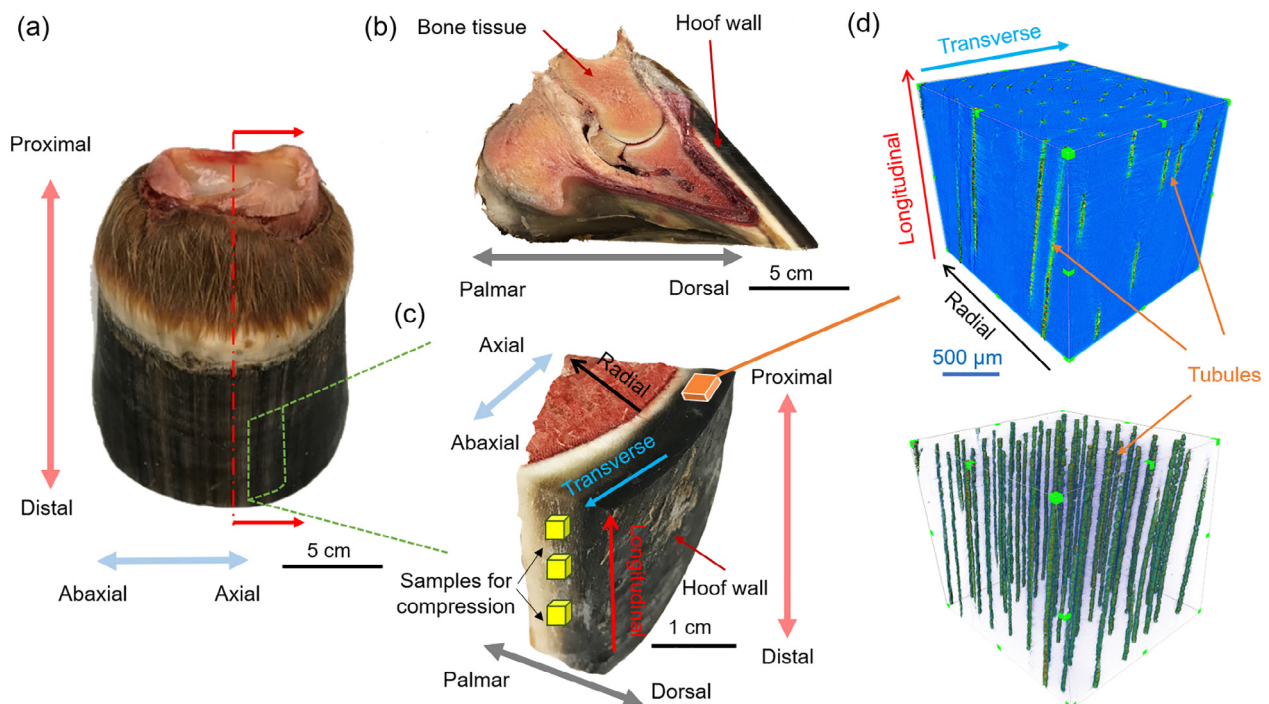


**Fig. 1.** Fresh horse hoof and tubular structures. (a and b) Dorsal view and midsagittal section from the proximal to distal aspects of a fresh hoof; (c) Transverse section in addition to the midsagittal section. Three directions are defined: longitudinal direction (proximal to distal); radial direction (axial to abaxial); transverse direction (tangential to hoof wall circumference in a transverse plane); (d) 3D reconstructed synchrotron x-ray micro-computed tomography image of hoof wall and the internal tubules.

## 2.2. Modulus and hardness mapping through nanoindentation

Nanoindentation has been used as an effective method to characterize the microscale mechanical properties of biological materials [41–43]. Samples ( $\sim 4 \times 4 \times 4$  mm cubes) from the same region as SEM and TEM samples were polished with the ultramicrotome prior to conducting nanoindentation tests. The loading direction was parallel with the distal-proximal (longitudinal) direction. Samples with different water content were tested (ambient dry, fresh and fully hydrated). Fresh samples were kept frozen before testing, while fully hydrated samples were immersed in DI water during testing. Nanoindentation experiments were conducted using a TI-950 TriboIndenter (Hysitron, Minneapolis, MN, USA) with a low-load transducer. Samples in the dried state were tested using a diamond cube corner probe while fresh and fully hydrated samples were tested using a fluid cell Berkovich probe. The two different tips were calibrated on the same standard quartz sample of known elastic modulus and a tip area profile was generated to accurately obtain a depth-contact area profile for each geometry. Thus, different geometry tips would accurately yield the same elastic modulus and hardness for a similar material. All maps featured a square array of indents ( $31 \times 31$  indents in dry and wet samples,  $10 \times 10$  indents in fresh samples) with a spacing of  $10 \mu\text{m}$  in orthogonal directions. The areas of maps were randomly chosen in the center of hoof wall covering both tubular and intertubular areas (Fig. S2). Different number of grids of the maps were chosen to cover both tubular and intertubular regions with the sample. Two maps of each condition were performed. Indents were controlled in displacement to a depth between 300 nm and 500 nm. The reason for choosing different depths for the maps is because the local sample topography (roughness) varies in the sample surface. To account for this, larger indent depths were chosen for rougher regions, so that the reported  $E_r$  and  $H$  values were accurate. A trapezoidal load function consisting of a 5 s load, 5 s hold, and 5 s unload was used for all mapping experiments.

## 2.3. Compression tests at different strain rates and failure surface imaging

Cubic samples ( $5 \times 5 \times 5$  mm) were randomly acquired from the central part of the thickness from proximal to distal locations on the hoof wall (Fig. 1c, yellow box). Compression tests at different strain rates ( $0.001 \text{ s}^{-1}$ ,  $0.01 \text{ s}^{-1}$ ,  $0.1 \text{ s}^{-1}$ ,  $1000 \text{ s}^{-1}$ ) were conducted in three different loading orientations (longitudinal, radial and transverse), using five samples for each orientation. A universal testing machine with a 30 kN load cell (Instron 3367 Dual Column Testing Systems, Instron, MA, USA) was used to conduct the low strain rates ( $0.001 \text{ s}^{-1}$ ,  $0.01 \text{ s}^{-1}$ ,  $0.1 \text{ s}^{-1}$ ) compression tests. High strain rate compression tests were performed with a split Hopkinson pressure bar system at an average strain rate of  $\sim 1000 \text{ s}^{-1}$ . The Young's modulus and yield strength in the stress strain curves were determined based on the methods mentioned in our previous study on horns [23,44]. Surfaces of the samples, before and after 30% quasi-static compression and impact in different directions, were imaged with Keyence VHX 1000 microscope (Keyence, Palatine, IL, USA).

## 2.4. Statistical analysis

Statistical analyses were performed to determine the significant differences (SSD) between the Young's modulus and yield strength in different loading orientations acquired from the compression tests. A one-way analysis of variance (ANOVA) method with Tukey's least significant difference procedure was applied [8]. The criterion for statistical significance was  $p < 0.05$ , which is the probability that there is no significant difference between the

results (Young's modulus and yield strength) from different experiments.

## 2.5. In-situ synchrotron X-ray computed tomography compression

Compressive deformation mechanisms of different materials at the microscale have been investigated by synchrotron tomography characterization, which has been found to be an effective method to study internal failures [45–47]. In this work, *in situ* quasi-static compression tests were conducted to study the failure and energy absorbent mechanism in the longitudinal direction (impact direction). The *in-situ* compression tests were carried out on the micro-tomography beamline 8.3.2 at the Advanced Light Source (Lawrence Berkeley National Laboratory, Berkeley, USA), using an x-ray accelerating voltage of 25 keV for the scans, with a field of view of  $3.3 \times 3.3$  mm at a resolution of  $1.3 \mu\text{m}$  per voxel. Two cubic samples with dimension  $2 \times 2 \times 2$  mm in the fresh and fully hydrated conditions were compressed longitudinally. The locations of the samples are in the similar regions as the samples tested in the compression tests to keep consistent. Scans were taken before tests and after the deformation at the strain of 30% and 60%. Amira software (FEI Visualization Sciences Group, Burlington, MA, USA) with a module of volume rendering was applied to reconstruct the 3D images.

## 3. Results and discussion

### 3.1. Hierarchical structure of equine hoof wall

Fig. 1d shows XCT images ( $0.65 \mu\text{m}$  resolution) of the axial region of the hoof wall. The 3D reconstruction indicates that the tubules are parallel to the longitudinal direction and are continuous from the proximal to distal end. The average area percentage of the medullary cavity is  $\sim 3\%$  with a diameter  $41 \pm 9 \mu\text{m}$  (Fig. S1). The hierarchical structure of equine hoof wall from micro- to nanoscale, characterized by XCT, optical and electron microscopy is shown in Fig. 2. Fig. 2a is a 3D reconstructed image in which the tubular areas show a higher material density. This indicates that the tubules absorb more  $\text{OsO}_4$  than the intertubular matrix, leading to their higher density. The tubular areas have elliptically-shaped cross sections with dimensions of  $\sim 206 \pm 24 \mu\text{m}$  (major axis) and  $107 \pm 15 \mu\text{m}$  (minor axis). The tubular areas accounted for  $\sim 30\%$  of the whole hoof wall cross section. To obtain further understanding of the cell shapes and arrangements in different regions, toluidine blue stained thin sections were imaged. Cell boundaries are clearly shown in Fig. 2b and c. Comparing the cell sizes and shapes in the tubules and intertubular matrix, significant differences were identified; irregular polygonal shapes were found in intertubular matrix area (red color), while cells were lens-shaped in the tubular areas (yellow color). The average cell size in the intertubular matrix is  $\sim 20 \pm 5 \mu\text{m}$ , while in the tubular region the cells are  $\sim 19 \pm 3 \mu\text{m}$  in length and  $\sim 5 \pm 1 \mu\text{m}$  thick. The longitudinal cross-section thin slice images are given in Fig. 2c. The tubular areas also had lens-shaped cells with dimension  $\sim 24 \pm 5 \mu\text{m}$  in length and  $\sim 4 \pm 1 \mu\text{m}$  in thickness, while irregular polygonal cell shapes with dimension  $\sim 17 \pm 5 \mu\text{m}$  were found in intertubular areas. By combining these longitudinal and cross-section images, the cell sizes and shapes in tubular and intertubular areas were obtained; the cells in intertubular areas are  $\sim 15$ – $25 \mu\text{m}$  irregular polyhedrons, while cells in tubular areas are thin lamellae with  $\sim 20 \mu\text{m}$  in diameter,  $\sim 5 \mu\text{m}$  in thickness, with the thickness direction perpendicular to and surrounding the tubules. This is the first study to report that there are differences between the cell sizes and shapes in the tubular and intertubular areas.

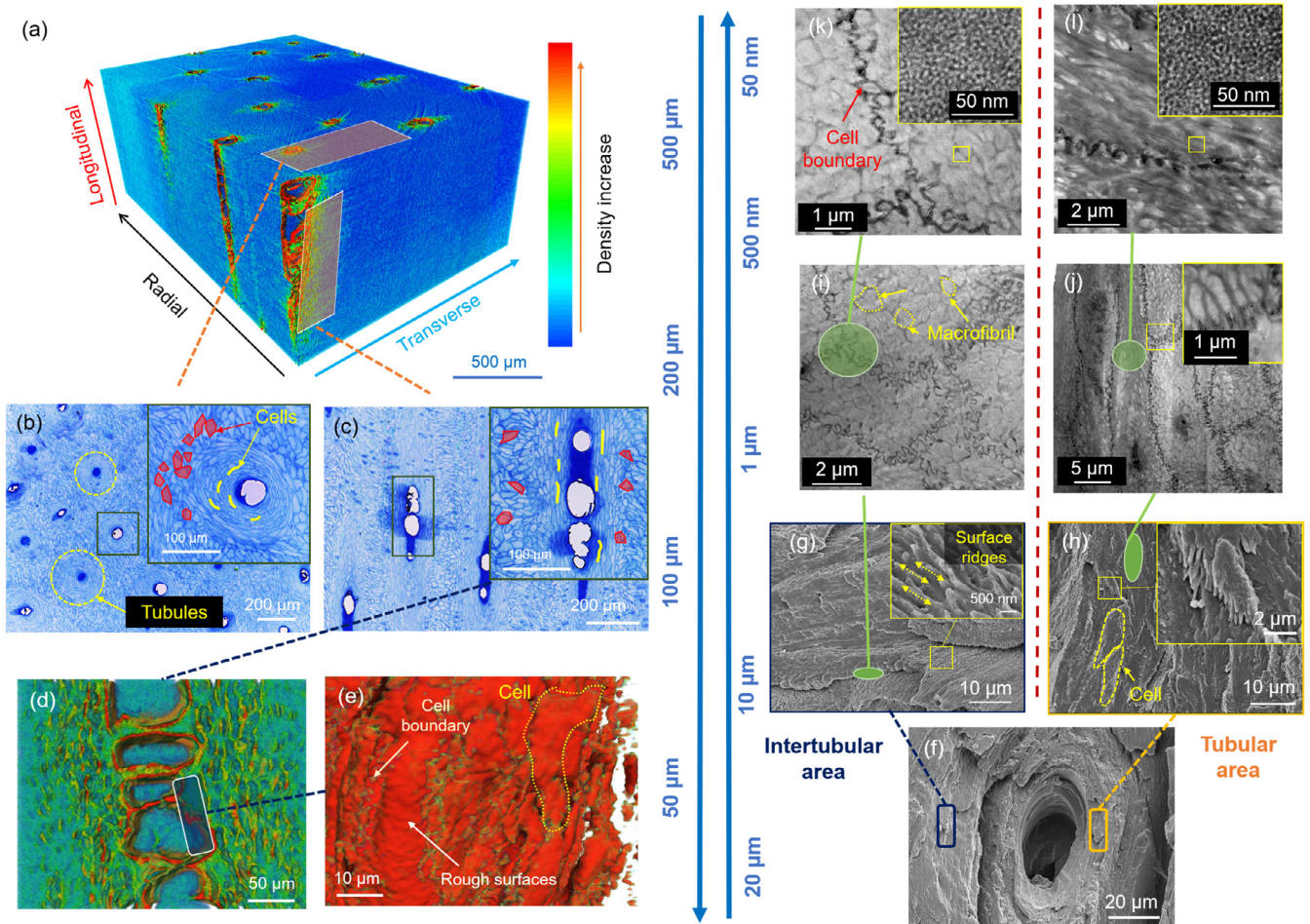


**Fig. 2.** Hierarchical structure of the hoof wall from micro- to nanoscale. (a) 3D reconstructed synchrotron x-ray micro-computed tomography (XCT) image of  $\text{OsO}_4$  stained hoof sample. Tubule areas show higher density indicating more  $\text{OsO}_4$  is stained in these areas. (b) Toluidine blue stained OM image of the cross section. Keratin cell shapes and sizes in both tubular (yellow) and intertubular areas (red) are shown in the green box at a higher magnification. The white holes inside the tubules are the longitudinal medullary cavities. (c) Toluidine blue stained optical microscopy image of longitudinal section of tubules. Cell shapes and dimensions are also shown in the green box at a higher magnification. (d) Longitudinal section of a single tubule, showing that the tubules are not hollow but have collapsed cell bridges inside. Cells in the tubular area are clearly shown due to the contrast of the cell boundaries. (e) 3D reconstructed image of the cells (yellow dash circle) in the tubular areas, showing cells stacking layer by layer. Cell boundaries are indicated in green color. (f) Scanning electron microscopy (SEM) image of freeze-fractured cross section of a single tubule. (g) Layered structure of keratin cells in intertubular areas. Rough cell surface is shown in the yellow box with a higher magnification. (h) Layered structure of keratin cells (yellow circle) in tubular areas and the cell boundaries. (i) Transmitted electron microscopy (TEM) image of cells and cell boundaries in intertubular areas. (j) TEM image of cells and cell boundaries in tubular areas. (k) TEM image of macrofibrils and intermediate filaments (IFs) in intertubular areas. (l) TEM image of macrofibrils and IFs in tubular areas. (For interpretation of the references to color in this figure legend, the reader is referred to the web version of this article.)

The tubule medullary cavities are not completely hollow. Thin bridges are found inside, which divide the medullary cavities into smaller chambers (Fig. 2d). Fig. 2e shows a 3D reconstructed image of a tubule wall, where the lamellar structure of cells (yellow dashed line) is indicated. The irregular green lines indicate cell boundaries that form a wavy (suture-like) structure. SEM images of freeze-fractured cross sections are shown in Fig. 2f–h. A concentric layered structure is found surrounding tubules in a higher magnification SEM image (Fig. 2f). Cells were also found with the same shape (Fig. 2h, yellow dashed lines), corroborating the findings from OM and XCT imaging. At a higher magnification (Fig. 2g), the cell surfaces are found to be quite rough with  $\sim 100$  nm thick ridges (yellow dashed arrows), which had been observed in the surfaces of the stratum corneum and pangolin scales [1]. This corresponds to the rough surface also found in the XCT image in Fig. 2e. More detailed structure and features of the cell boundaries and cytoskeleton were characterized with TEM (Fig. 2i–l). Fig. 2i shows TEM images of the cell morphology in the intertubular areas. Suture structured cell boundaries are identified as the dark, wavy lines, due to more  $\text{OsO}_4$  staining.

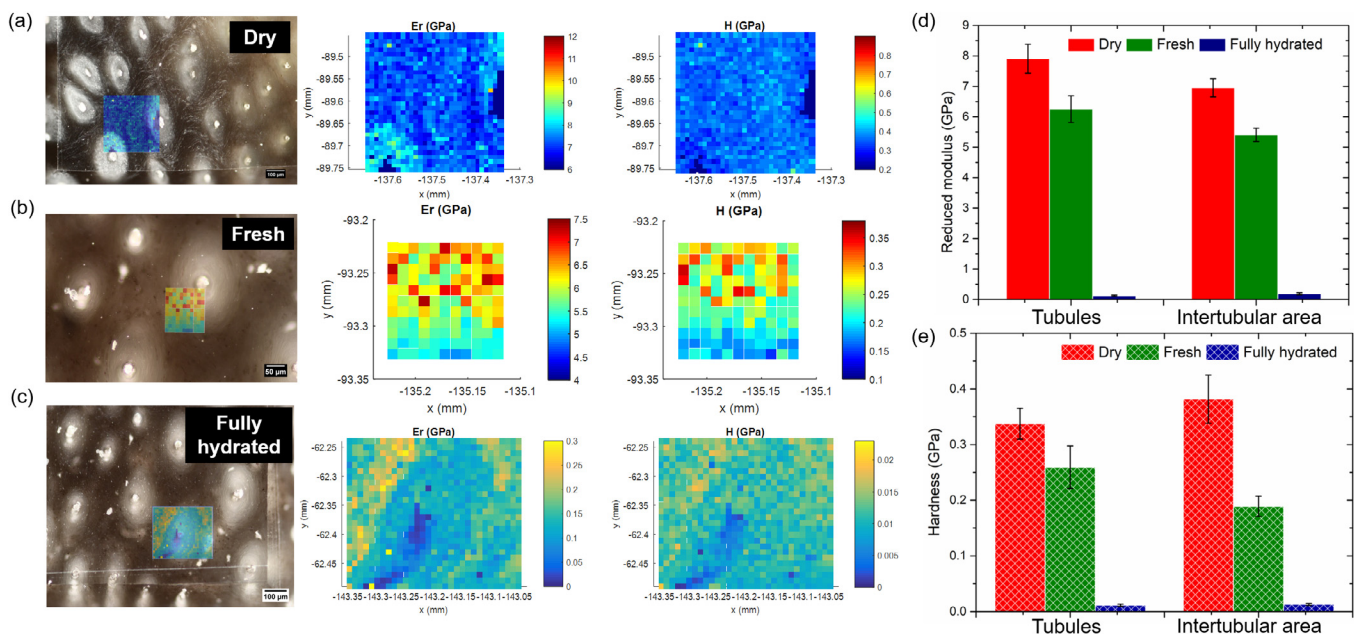
Macrofibrils with an average diameter of  $\sim 710 \pm 130$  nm were found inside the cells (Fig. 2i), which is larger than that in hair fibers ( $\sim 100$ – $400$  nm) and horns ( $\sim 200$  nm) [8,48]. This larger diameter of the macrofibrils may generate a higher stiffness compared to that of the smaller fibrils, based on previous studies on hair [49]. In Fig. 2j, the cells in the tubular area are elliptically-shaped with dimension  $\sim 20$   $\mu\text{m}$  in length and  $\sim 5$   $\mu\text{m}$  in thickness, which verified the findings in the OM studies. Detailed images of the macrofibril in cross section show them not to be circular, which indicates the macrofibrils are not perfectly aligned along the tubule (longitudinal) direction (Fig. 2l). IFs (white dots,  $\sim 7$ – $10$  nm in diameter) embedded in an amorphous matrix in the intertubular and tubular areas are shown in Fig. 2k and l (yellow box), respectively. The percentage of intermediate filaments are different in these two areas:  $\sim 32.2\%$  in the intertubular area and  $\sim 21.3\%$  in the tubular area, which is similar to results in previous studies [30]. The cells in tubular area (Fig. 2l) are darker than that in intertubular areas (Fig. 2k) because more  $\text{OsO}_4$  is concentrated in the tubular area, due to the higher fraction of amorphous matrix.

In summary, a tubular structure was identified in the equine hoof wall. The medullary cavity inside the tubules were not completely hollow but had thin bridges forming chambers. Keratin cells formed irregular polyhedrons in intertubular areas and changed to ellipsoid-shaped in tubular areas. There is no preferred orientation of the microfibrils in both tubular and intertubular areas. At the nanoscale, crystalline IFs ( $\sim 7\text{--}10\text{ nm}$ ) embedded in an amorphous matrix were found in both tubules and intertubular areas, while the intertubular areas had a higher IF fraction.

### 3.2. Multi-scale mechanical behavior of equine hoof wall

From previous work [8,35,50], the mechanical properties of big horn sheep horns have been found to depend markedly on the level of hydration. Accordingly, nanoindentation tests were subsequently conducted on samples at three hydration states: ambient dry, fresh and fully hydrated. The reduced modulus ( $E_r$ ) and hardness ( $H$ ) maps were acquired at the three hydration states to determine the differences between the tubular and intertubular regions. Fig. 3a–c show the reduced modulus and hardness maps. Fig. 3d summarizes the reduced modulus of both tubular and intertubular areas in the different hydration states. In the dry condition,  $E_r \sim 8.0 \pm 0.5\text{ GPa}$  in tubular areas and  $\sim 7.0 \pm 0.3\text{ GPa}$  in intertubular areas. In the fresh ( $\sim 30.2\text{ wt\% H}_2\text{O}$ ) condition  $E_r \sim 6.3 \pm 0.4\text{ GPa}$  in tubular areas and  $\sim 5.4 \pm 0.2\text{ GPa}$  in intertubular areas. This suggests that tubules reinforce the intertubular areas. In the fully hydrated condition,  $E_r$  decreased to  $0.12 \pm 0.02\text{ GPa}$  in the tubular areas and  $0.19 \pm 0.02\text{ GPa}$  in the intertubular areas, values that are orders of magnitude smaller than in the dry and fresh conditions. A similar trend was also found in hardness measurements (Fig. 3e).  $H$  values in tubular and intertubular areas in the dry condition were similar, respectively,  $\sim 0.34 \pm 0.03\text{ GPa}$  and  $\sim 0.38 \pm 0.03\text{ GPa}$ . For the fresh condition, corresponding  $H$  values in tubular areas ( $\sim 0.26 \pm 0.04\text{ GPa}$ ) were higher than that in intertubular areas ( $0.19 \pm 0.02\text{ GPa}$ ). In the fully hydrated ( $\sim 40\text{ wt\% H}_2\text{O}$ ) condition,  $H$  values in the tubular and intertubular areas were again similar, specifically,  $0.011 \pm 0.002\text{ GPa}$  and  $0.013 \pm 0.002\text{ GPa}$ , respectively, but are orders of magnitude smaller than for the dry and fresh conditions.

In summary, both  $E_r$  and  $H$  in the tubular and intertubular areas decreased significantly after full hydration. There is only  $\sim 20\%$  decrease in  $E_r$  and  $H$  from the dry to fresh samples, but almost  $\sim 98\%$  decrease from fresh to fully hydrated samples. This indicates that water effects dominate the mechanical properties once the tissue is fully hydrated. It was also found that the tubular area had higher  $E_r$  than the intertubular areas in both dry and fresh conditions, while the opposite trend was found in the fully hydrated condition. This can be explained by the basic composition in these two areas in that the tubular areas have a greater fraction of the amorphous matrix. Based on previous work [16,51], the amorphous matrix has a higher amount of cystine, which is a sulfur-rich amino acid. The enriched disulfide bonds between the IF-matrix and matrix-matrix could lead to higher rigidity and mechanical stiffness in the tubule areas [52,53]. Thus, the tubules are stiffer than the intertubular areas, which act as a ‘fiber’ reinforced component in the structure. These findings are different from results found in the previous studies [34,54], where it was concluded that it was the intertubular matrix that accounted for the mechanical strength and stiffness, while the tubules were only acting as crack-arresting stopping interfaces. After full hydration, the stiffness of amorphous matrix decreased significantly due to water incorporation, while the crystalline IFs were not affected [29,55–57], leading to a greater decrease of  $E_r$  in the tubular areas due to the higher fraction of the amorphous matrix.  $H$  remained constant in the dry samples (Fig. 3a) indicating that the ability for local plastic deformation in different regions was similar. While in both the fresh and fully hydrated samples, the trends of  $H$  maps are similar as that of  $E_r$  maps (Fig. 3b and c), showing that after hydration the resistance to local plastic deformation is more sensitive to modulus changes, consistent with the behavior of most biological materials [58]. Indentation hardness is the hybrid measurement of the resistance to both elastic and plastic deformation, while the elastic modulus quantifies the elastic deformation [58]. The different trends between the hardness and elastic modulus maps under dry conditions indicate the plastic deformation dominates the tests, which is reasonable because keratin materials are brittle without water molecule ‘‘plasticizers,’’ and more plastic deformation will be produced than elastic deformation [1].



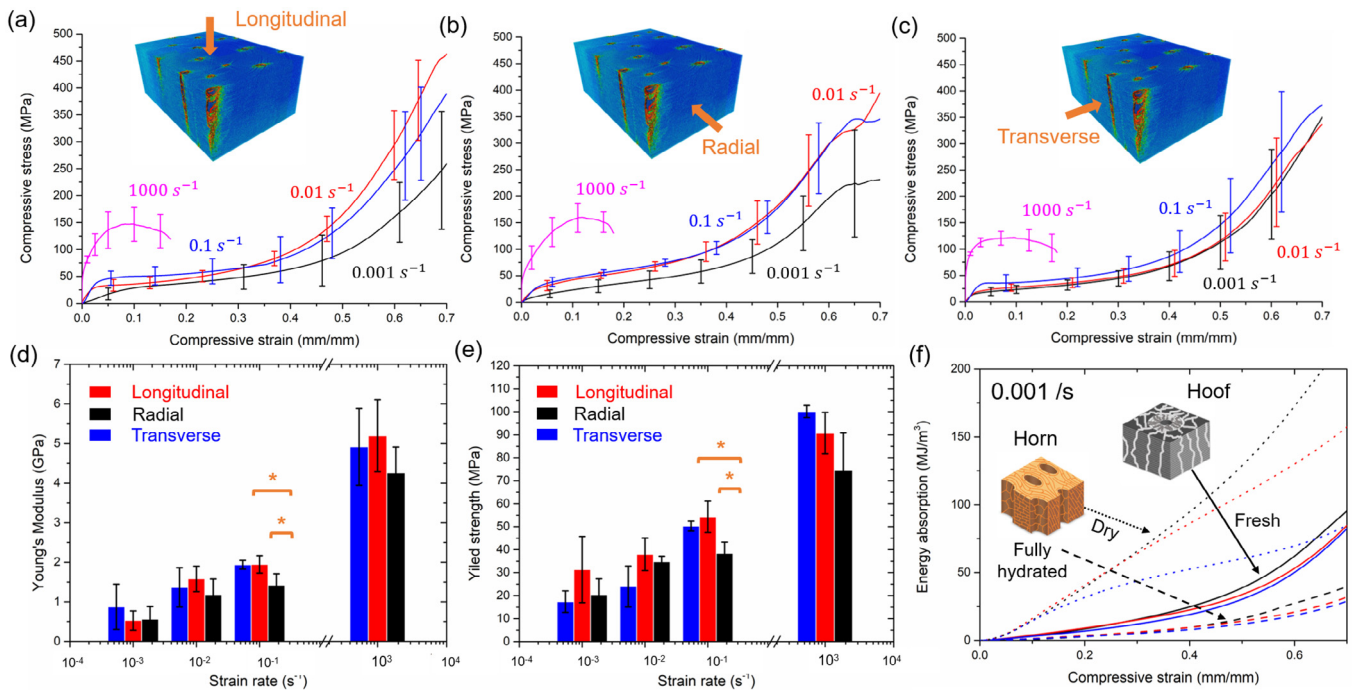
**Fig. 3.** Nanoindentation characterization of the transverse sections perpendicular to the tubules. (a–c) Reduced modulus ( $E_r$ ) and hardness ( $H$ ) maps of the horse hoof wall in ambient dry, fresh and fully hydrated conditions. (d) Comparison of  $E_r$  in tubule and intertubular areas in the dry, fresh and fully hydrated conditions. (e) Comparison of  $H$  in tubule and intertubular areas in the dry, fresh and fully hydrated conditions.

Fig. 4a–c show the compressive stress-strain curves in different orientations and strain rates. The stress-strain curves indicate that the hoof is an ideal energy absorption material with similar representative compression behavior of traditional cellular and foam structures [59,60]. At low strain rates ( $10^{-3}\text{s}^{-1}$ ,  $10^{-2}\text{s}^{-1}$ ,  $10^{-1}\text{s}^{-1}$ ), the shapes of the stress-strain curves begin with an initial elastic region that is followed by a region with an extended plateau, which is where the main energy absorption occurs, before a final densification region where the stress increases significantly. At a higher strain rate ( $10^3\text{s}^{-1}$ ), the samples were able to survive after  $\sim 20\%$  deformation and recovered their original shapes after high-speed impacts in all the three directions. The Young's modulus and yield strength of the hoof samples under different loading orientations and strain rates are shown in Fig. 4d and e. Both increase as the strain rate increases. This strain-rate dependent behavior is due to the viscoelastic property of keratin, which has been studied in human hair and bighorn sheep horn [20,50]. No statistically significant difference was found between the Young's modulus and yield strength among the three different loading orientations at strain rate  $10^{-3}\text{s}^{-1}$  and  $10^{-2}\text{s}^{-1}$ . While loading at a strain rate  $10^{-1}\text{s}^{-1}$ , both the Young's modulus and yield strength were lower in radial direction than the other two directions. This could be due to the collapse of tubules when compressed radially [8,23]. By integrating the compressive stress-strain curves, the amount of energy absorption as a function of compressive strain at the strain rate  $10^{-3}\text{s}^{-1}$  can be calculated and is plotted in Fig. 4f. For comparison, the energy absorption of the bighorn sheep horn with the same amount of water content (fully hydrated  $\sim 30\%$  wt%) and ambient dry condition ( $\sim 10\%$  wt%) is also shown [8]. More than 88% of the total energy were dissipated by plastic deformation and viscoelasticity of keratin based on the loading and unloading curves of fresh hoof samples (Fig. S3). Similar unloading behavior was also found in horn samples in previous study, indicating most of the compressive deformation are irreversible. It was found that hoof samples

absorb more energy than bighorn sheep horn in all the three loading directions under quasi-static loading at the same hydration level. The average energy absorption in the hoof after 70% deformation was  $87.6\text{ MJ/m}^3$ , which was  $\sim 2.6$  times of the energy absorption in bighorn sheep horn.

### 3.3. Failure and energy absorption mechanisms

Failure mechanisms under compression were studied in detail with both OM and *in-situ* synchrotron XCT methods to understand the energy absorption mechanisms (deformation modes) in the three different directions. OM images of the cross-sections in the longitudinal (Fig. 5a), radial (Fig. 5b) and transverse (Fig. 5c) directions were examined before and after 30% quasi-static (strain rate  $10^{-3}\text{s}^{-1}$ ) compression (Fig. 5d–f). No obvious damage to the microstructure was observed but small cracks in the tubular region were found in the sample when compressed in the longitudinal direction (Fig. 5d). Cracks in diagonal directions (black dashed arrows in Fig. 5e) were found inside each tubule when compressed in radial direction. Cracks were only observed in the tubule areas (Fig. 5e). In the transverse direction, small cracks (black dashed arrow) start propagating from the vertices of one elliptically-shaped tubule to another, forming long cracks (Fig. 5f). Compared with the bighorn sheep horn, no shear bands or catastrophic failures were observed in hoof samples [8]. From previous work on big horn sheep horns [8], shear bands, together with lamellae buckling formed that caused catastrophic structural failure when compressed and impact longitudinally. While in the hoof, the tubules protect the structure from shear-banding, due to the higher stiffness in the tubular areas. Fig. 5g–i show the failure surfaces after high strain rate ( $10^3\text{ s}^{-1}$ ) impacts in longitudinal, radial and transverse direction, respectively. Cracks were observed in samples after impact in all the three directions. The cracks propagated in the intertubular areas, while no cracks or other damage



**Fig. 4.** Compressive stress-strain curves of fresh hoof samples ( $\sim 30\%$   $\text{H}_2\text{O}$ ) in different loading orientations and strain rates; (a) Longitudinal, (b) radial and (c) transverse. Comparison of (d) Young's modulus and (e) yield strengths, both at different strain rates and loading orientations. One-way ANOVA tests were conducted for the different directions at different strain rates. “\*\*” refers to statistical significant difference between the results with the level of 0.05. (f) Variation on energy absorption (area under the stress-strain curve) as a function of compressive strain in hoof (fresh  $\sim 30\%$   $\text{H}_2\text{O}$ ) and horn (fully hydrated  $\sim 30\%$   $\text{H}_2\text{O}$ , ambient dry  $\sim 10\%$   $\text{H}_2\text{O}$ ) [8] in different loading orientations (red: longitudinal, black: radial, blue: transverse). (For interpretation of the references to color in this figure legend, the reader is referred to the web version of this article.)

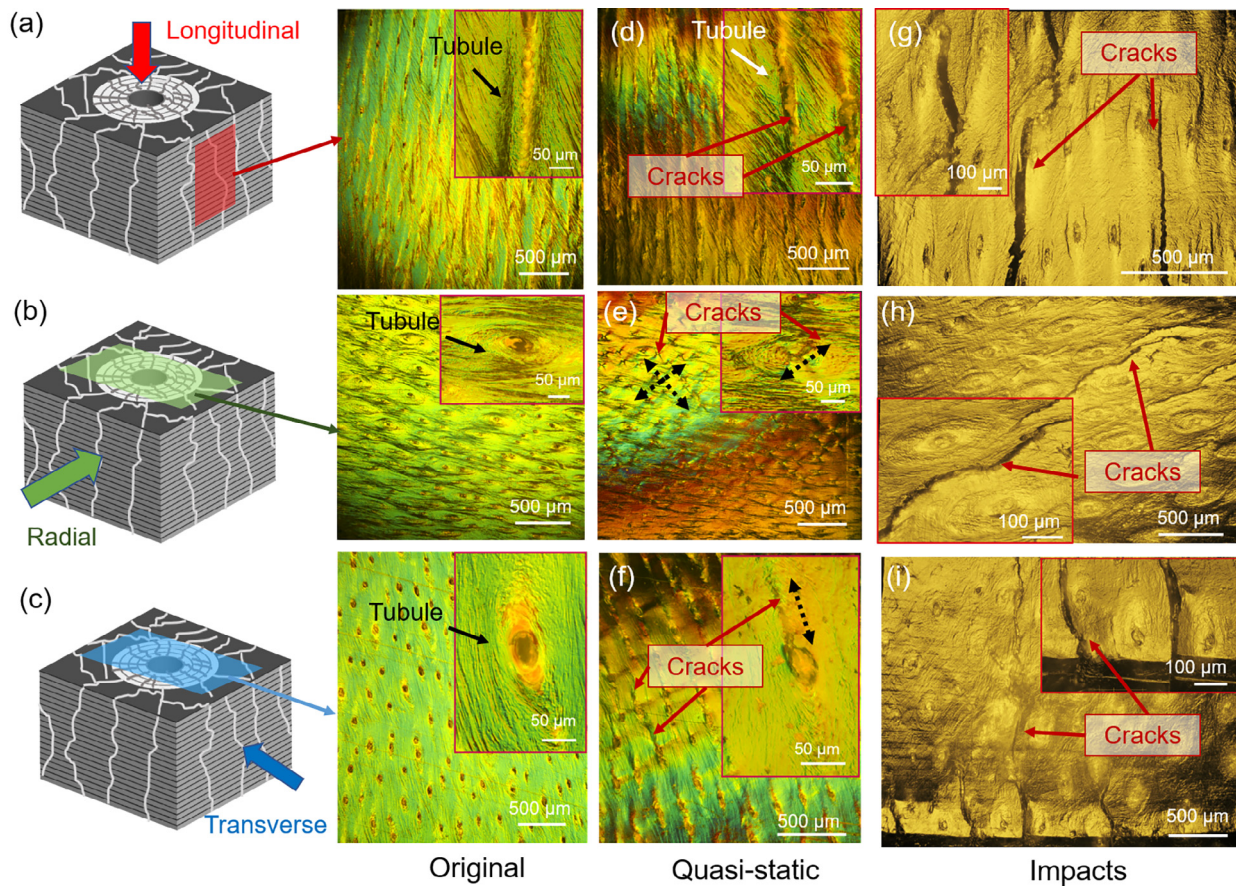


**Fig. 5.** Deformation and failure mechanisms before and after 30% quasi-static compression and impact loading. (a–c) Optical microscopy images of samples surfaces before compression in the different loading orientations: longitudinal section (red color surface in (a)) when loading longitudinally; cross sections (green color surface in (b) and blue color surface in (c)) when loading radially and transversely. (d–f) Surface images after 30% quasi-static compression in longitudinal, radial and transverse direction, respectively. Cracks are observed in the tubule areas in all the three directions. Black dashed lines in (e) and (f) indicate the crack directions. (g–i) Surface images after impact at a strain rate  $\sim 1000 \text{ s}^{-1}$  in longitudinal, radial and transverse direction, respectively. Cracks are observed in the intertubular areas. No damage is found in the tubular areas. (For interpretation of the references to color in this figure legend, the reader is referred to the web version of this article.)

were observed in the tubular areas. This indicated the tubules in hoof samples were able to redirect crack propagation under impact due to their higher stiffness than the intertubular areas. When the horse is galloping, the main loading comes from the ground and is applied along the longitudinal direction. To examine this, the deformation of the tubules was studied in the longitudinal direction with *in situ* XCT compression tests. Fig. 6 shows the 3D reconstructed images of fresh hoof samples before (Fig. 6a–c) compression and compressed at the strain of 30% (Fig. 6d–f) and 60% (Fig. 6g–i). Fig. 6b and c show the proximal and abaxial views of the samples before compression. A higher magnification image indicates that tubules consist of segments of cells (Fig. 6c). After 30% compression in the longitudinal direction, the tubules are buckled (Fig. 6d). The proximal and abaxial view of the buckled tubules are shown in Fig. 6e and f, where clear curvature of the tubules are observed. In Fig. 6f, cracks on the tubules are found after compression, which can be correlated to previous findings shown in Fig. 5d. Interestingly, in Fig. 5d, no buckling of tubules is found in the OM image after 30% compressive strain, only cracks are observed in the tubules. These findings suggest that the buckling of tubules may recover once the load is released, indicating a viscoelastic behavior. Fig. 6g–k shows images after 60% compression. Few tubules can be found in Fig. 6g. From the proximal and abaxial view of the sample (Fig. 6h and i), it can be found that the buckled tubules become discontinuous and apparently disappear, indicating densification under compression. Fig. 6i shows severe damage, in which the tubules are found along a diagonal

direction (red dashed line) due to buckling. Cracks (red box) and cell shear and shape changes (Fig. 6i, yellow dashed line) in the tubules, compared to the undeformed cells (Fig. 6c, yellow dashed line), are observed due to the shear forces on the tubules. This indicates that at 60% compression, the buckled tubules have compressed and densified within the intertubular matrix, leading to the disappearance of the tubules. This densification can be correlated to the stress-strain curves in Fig. 4a, in which a sharp increase of the stress occurs around 60% strain due to this densification. Fig. 6j shows 3D reconstructed block image and tubules after 30% compression in the fully hydrated condition. No buckling of the tubules was observed; only cracks were found in the tubules. This indicates the tubules are no longer serving as reinforcing structures due to the stiffness decrease after hydration (Fig. 3). After 60% compression, no tubules are found, which is attributed to densification. Therefore, buckling and cracking of the tubules are the main deformation and energy absorption mechanisms in the fresh equine hoof when compressed longitudinally. Due to the higher stiffness and yield strength of the tubules, more energy will be absorbed because of this tubule-reinforced structural designs. However, hoof samples in the fully hydration state lose this tubule reinforcement.

#### 3.4. Comparisons between the equine hoof and the bighorn sheep horn

Based on the present study and previous reports [8,50], it can be concluded that both equine hooves and bighorn sheep horns are

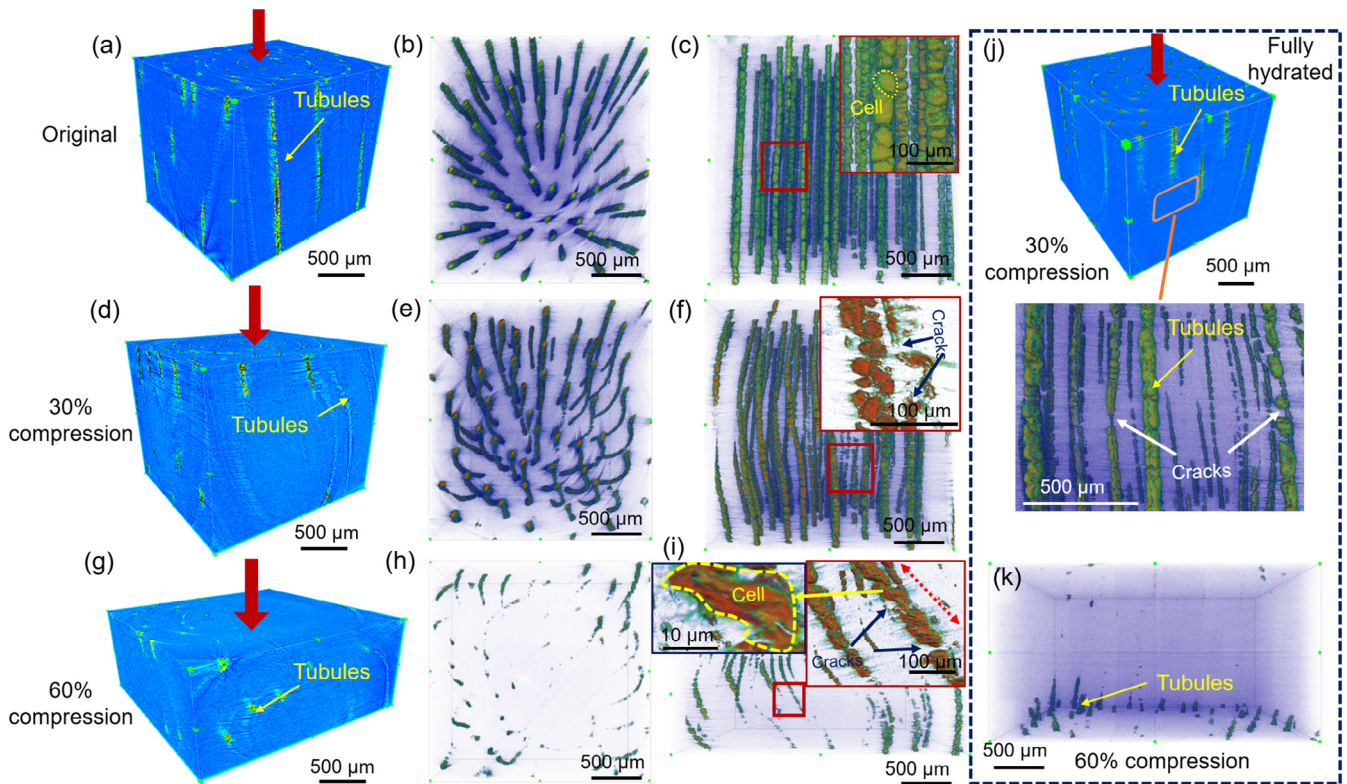


**Fig. 6.** *In-situ* synchrotron x-ray computed tomography (XCT) compression of fresh and fully hydrated hoof samples. (a) 3D reconstructed XCT image of the undeformed sample. (b) Proximal view of the undeformed sample showing the tubules. (c) Abaxial view of the undeformed tubules. Higher magnification image of tubules shows keratin cells surrounding the chambers of medullary cavities. (d) 3D reconstructed XCT image of the sample after 30% compression in the longitudinal direction. (e) Proximal view after 30% deformation, where buckling of tubules are shown. (f) Abaxial view of buckled tubules at 30% deformation. Cracks in the tubules are also observed in the higher magnification image. (g) 3D reconstructed XCT image after 60% compression in the longitudinal direction. (h) Proximal view after 60% deformation. Tubules start disappearing due to the severe deformation. (i) Abaxial view of severely buckled tubules. Tubules have collapsed and compressed after 60% compression. Red dashed arrow indicates longitudinal tubule is severely buckled in the diagonal direction. (j) 3D reconstructed XCT image of a fully hydrated hoof sample after 60% deformation. No buckling of tubules is observed. The tubules start and cracking. (k) No tubules are observed after 60% deformation in the fully hydrated samples, indicating tubules have collapsed and merged with the intertubular matrix. (For interpretation of the references to color in this figure legend, the reader is referred to the web version of this article.)

impact resistant and energy absorbent. Both the horn and hoof are composed of  $\sim 100\%$  keratin and have tubular structural features. The tubules and viscoelastic properties of keratin contribute to the energy absorption and impact resistance [8,23,35,40]. Although both horn and hoof are designed for energy absorption and impact resistance, differences in the actual loading direction, material composition and structural designs are found in the current study, which leads to the differences in energy absorption. In terms of the materials compositions, one of the important factors that affect the mechanical properties significantly is the hydration state [35,50]. Water content in fresh horns are somewhere between  $\sim 15$  wt% and 20 wt%, while fresh equine hoof has  $\sim 30$  wt%, which is similar to the fully hydrated horns [55]. In terms of the structural designs, the hoof has a more complicated tubular structure, consisting of  $\sim 30\%$  volume percent of the reinforced tubular area, while this is not found in the horn. Due to the tubule reinforcement, the hoof shows similar energy absorption amount and energy dissipation mechanisms (fracture and failure limited in tubules) in different directions, while bighorn sheep horn shows anisotropic failure [8]. In horns, the radial direction (perpendicular to the tubules) has higher energy absorption than the other two directions [8]. The hoof shows  $\sim 2.6$  times higher energy absorption than horns at the same hydration level under quasi-static compression. However, in the natural condition, the water content in fresh horn is smaller than in the hoof. In Fig. 4f, the upper (ambient dry) and lower (fully hydrated) that limit amount of energy absorption in fresh horn are indicated. Thus, in natural fresh horns, the energy

absorbent abilities in the radial direction are comparable with fresh hooves. While under high strain rate ( $\sim 10^3$  s $^{-1}$ ) impacts, both dry and wet horn samples undergo much higher plastic deformation (more than 60%) than that in hoof ( $\sim 20\%$ ), leading to more energy absorption in horn samples (Fig. S4). Thus, the tubular designs in horn is better for energy absorption caused by high strain rate impacts because of the large plastic deformation, while the reinforced tubular structure in hoof acts as a role protecting the hoof from catastrophic failure from cyclic low strain-rate loadings.

#### 4. Conclusions

The hierarchical structure, multi-scale mechanical behavior and energy absorption mechanisms of equine hoof walls under compression were investigated. The hierarchical structure was examined by optical (OM) and scanning and transmission electron microscopy as well as high-resolution synchrotron X-ray computed tomography (XCT). Multi-scale mechanical analysis was evaluated using nanoindentation and compression tests at different strain rates. Failure and energy absorption mechanisms of hoof samples under compression were studied with OM and *in situ* compression tests with XCT. The main conclusions from this study are:

- Tubules embedded in the intertubular matrix were identified in the transverse cross-section. The total porosity was  $\sim 3\%$  (medullary cavity), with the tubules comprising  $\sim 30\%$  of the whole area. For the first time we report that the sizes and

shapes of the keratin cells were different in the tubular and intertubular regions: cells in intertubular areas are irregular polygons  $\sim 20 \pm 5 \mu\text{m}$ , while cells in tubular areas are lamellar  $\sim 19 \pm 3 \mu\text{m}$  in diameter,  $\sim 5 \pm 1 \mu\text{m}$  in thickness with the thickness direction perpendicular to the tubules. The differences of sizes and shapes of cells between these two regions are due to the different cell growth mechanisms. The mechanical implications of the cell shapes and sizes are currently unclear and need to be further studied. The intertubular matrix shows a higher amount of IFs (32.2%) while the tubular area has a lower value (21.3%).

- The stiffness and hardness of the tubular areas were higher than that in the intertubular areas in both the dry and fresh hoof samples. This indicates that the tubules serve as reinforced structures to support the load. When the samples are fully hydrated, the stiffness and hardness of tubules are smaller than in the intertubular areas, which is due to the higher water absorption in the tubular areas. The overall compression behavior shows a strain rate dependency and isotropy. Full hydration leads to a 98% decrease of the modulus and hardness over that of fresh hoof samples.
- The compressive mechanical properties show isotropy when loading at strain rates at  $10^{-3} \text{ s}^{-1}$  and  $10^{-2} \text{ s}^{-1}$ , while the stiffness and strength were lower when compressed radially than compressed in the other two directions at a strain rate  $10^{-1} \text{ s}^{-1}$ . Elastic buckling and fracture of the tubules are the main failure and energy absorption mechanisms when compressed longitudinally quasi-statically. The reinforced tubules protect the whole hoof structure from shear-banding or developing cracks in all the three directions, leading to a higher energy absorption compared with bighorn sheep horn at the same hydration level.
- Hoof wall samples can survive and recover to their original dimensions after impacts in different directions at a strain rate  $\sim 10^3 \text{ s}^{-1}$ . Tubules are able to redirect crack propagation thus protecting the hoof samples from catastrophic failures under high-speed impacts.

In the present study, it is verified that the hoof wall shows energy absorption properties under low strain rate ( $10^{-3} \text{ s}^{-1} \sim 10^{-1} \text{ s}^{-1}$ ) compression and could also survive without noticeable damage and deformation under high-speed impacts (strain rate  $10^3 \text{ s}^{-1}$ ) under different loading orientations. The energy absorbent and impact resistant properties found in hoof wall are correlated to the material and structural designs. The findings in this work presented and identified a natural tubule reinforced polymer composite structure in the equine hoof, which can absorb a large amount of energy and resist high-speed impacts without catastrophic structural failure. Cracking and deformation of tubules dissipate energy while protecting the matrix from fracture or damage, even after 60% compressive strain under quasi-static loading. Under high-speed impacts, the stiff and strong tubules (relative soft matrix) act as crack deflectors to avoid whole structural failure. Thus, the results here may inspire designs of light weight energy absorbent and impact resistant synthetic structure and materials. More specifically, light weight energy absorbent materials and structural designs could potentially provide effective protective systems to the vehicles and increase road safety, while reducing the fuel consumption from an environmental perspective [61].

## Acknowledgements

The authors gratefully acknowledge financial support from a Multi-University Research Initiative through the Air Force Office of Scientific Research (AFOSR-FA9550-15-1-0009) and a National Science Foundation Biomaterials Grant (1507978). We also

acknowledge the use of beamline 8.3.2 with the assistance from Dula Parkinson and Harold Barnard at the Advanced Light Source at the Lawrence Berkeley National Laboratory, which is supported by the Office of Science, Office of Basic Energy Sciences, Division of Materials Sciences and Engineering of the U.S. Department of Energy under contract no. DE-AC02-05CH11231, and thank Eric Bushong and Mason Mackey at National Center for Microscopy and Imaging Research (NCMIR), Timo Meerloo and Ying Jones at Electron Microscopy Facility at UC San Diego for providing the help with the tomography and TEM sample preparation and imaging. We also thank Ryan Anderson of the Nano3 Laboratory of Calit2 for helping with the SEM and optical microscopy, and Prof. Marc A. Meyers from UC San Diego for his kind and enthusiastic support of this project. This work was performed in part at the San Diego Nanotechnology Infrastructure (SDNI) of UCSD, a member of the National Nanotechnology Coordinated Infrastructure, which is supported by the National Science Foundation (Grant ECCS-1542148).

## Appendix A. Supplementary data

Supplementary data to this article can be found online at <https://doi.org/10.1016/j.actbio.2019.04.003>.

## References

- [1] B. Wang, W. Yang, J. McKittrick, M.A. Meyers, Keratin: structure, mechanical properties, occurrence in biological organisms, and efforts at bioinspiration, *Prog. Mater. Sci.* 76 (2016) 229–318.
- [2] J. McKittrick, P.Y. Chen, S.G. Bodde, W. Yang, E.E. Novitskaya, M.A. Meyers, The structure, functions, and mechanical properties of keratin, *JOM* 64 (2012) 449–468.
- [3] P.Y. Chen, J. McKittrick, M.A. Meyers, Biological materials: functional adaptations and bioinspired designs, *Prog. Mater. Sci.* 57 (2012) 1492–1704.
- [4] M.A. Meyers, J. McKittrick, P.Y. Chen, Structural biological materials: critical mechanics-materials connections, *Science* 339 (2013) 773–779.
- [5] J. McKittrick, P.Y. Chen, L. Tombolato, E.E. Novitskaya, M.W. Trim, G.A. Hirata, E.A. Olevsky, M.F. Horstemeyer, M.A. Meyers, Energy absorbent natural materials and bioinspired design strategies: a review, *Mater. Sci. Eng. C-Mater. Biological Appl.* 30 (2010) 331–342.
- [6] L.J. Gibson, M.F. Ashby, G.N. Karam, U. Wegst, H.R. Shercliff, “The mechanical-properties of natural materials .2. Microstructures for mechanical efficiency,” *Proc. R. Soc.-Math. Phys. Sci.* 450 (1995) 141–162.
- [7] U.G.K. Wegst, M.F. Ashby, The mechanical efficiency of natural materials, *Phil. Mag.* 84 (2004) 2167–2181.
- [8] W. Huang, A. Zaheri, J.Y. Jung, H.D. Espinosa, J. McKittrick, Hierarchical structure and compressive deformation mechanisms of bighorn sheep (*Ovis canadensis*) horn, *Acta Biomater.* 64 (2017) 1–14.
- [9] Courtney M, Courtney A, “Sheep collisions: The good, the bad, and the tbi,” arXiv preprint arXiv:0711.3804, (2007).
- [10] A. Kitchener, An analysis of the forces of fighting of the blackbuck (*Antelope cervicapra*) and the bighorn sheep (*Ovis canadensis*) and the mechanical design of the horn of bovids, *J. Zool.* 214 (1988) 1–20.
- [11] J. Lanovaz, H. Clayton, L. Watson, In vitro attenuation of impact shock in equine digits, *Equine Vet. J.* 30 (1998) 96–102.
- [12] J.J. Setterbo, T.C. Garcia, I.P. Campbell, J.L. Reese, J.M. Morgan, S.Y. Kim, M. Hubbard, S.M. Stover, Hoof accelerations and ground reaction forces of thoroughbred racehorses measured on dirt, synthetic, and turf track surfaces, *Am. J. Vet. Res.* 70 (2009) 1220–1229.
- [13] K. Parsons, A. Spence, R. Morgan, J. Thompson, A. Wilson, High speed field kinematics of foot contact in elite galloping horses in training, *Equine Vet. J.* 43 (2011) 216–222.
- [14] N. Crevier, D. Robin, P. Pourcelot, S. Falala, L. Holden, P. Estoup, L. Desquilbet, J. Denoix, H. Chateau, Ground reaction force and kinematic analysis of limb loading on two different beach sand tracks in harness trotters, *Equine Vet. J.* 42 (2010) 544–551.
- [15] E. Barre, B. Landjerit, R. Wolter, “Shock, and vibration during the hoof impact on different track surfaces,” *Training* 1 (1991) 94–96.
- [16] J. Hearle, A critical review of the structural mechanics of wool and hair fibres, *Int. J. Biol. Macromol.* 27 (2000) 123–138.
- [17] R. Fraser, T. MacRae, A. Miller, The coiled-coil model of  $\alpha$ -keratin structure, *J. Mol. Biol.* 10 (1964) 147–156.
- [18] R.B. Fraser, D.A. Parry, Intermediate filament structure in fully differentiated (oxidized) trichocyte keratin, *J. Struct. Biol.* 200 (2017) 45–53.
- [19] R. Fraser, T. MacRae, E. Suzuki, Structure of the  $\alpha$ -keratin microfibril, *J. Mol. Biol.* 108 (1976) 435–452.
- [20] Y. Yu, W. Yang, B. Wang, M.A. Meyers, Structure and mechanical behavior of human hair, *Mater. Sci. Eng. C-Mater. Biological Appl.* 73 (2017) 152–163.

- [21] Y. Seki, S.G. Bodde, M.A. Meyers, Toucan and hornbill beaks: a comparative study, *Acta Biomater.* 6 (2010) 331–343.
- [22] R. Caputo, G. Gasparini, D. Contini, A freeze-fracture study of the human nail plate, *Arch. Dermatol. Res.* 272 (1981) 117–125.
- [23] L. Tombolato, E.E. Novitskaya, P.Y. Chen, F.A. Sheppard, J. McKittrick, Microstructure, elastic properties and deformation mechanisms of horn keratin, *Acta Biomater.* 6 (2010) 319–330.
- [24] M. Ryder, Structure of rhinoceros horn, *Nature* 193 (1962) 1199.
- [25] Z. Liu, D. Jiao, Z. Weng, Z. Zhang, Structure and mechanical behaviors of protective armored pangolin scales and effects of hydration and orientation, *J. Mech. Behav. Biomed. Mater.* 56 (2016) 165–174.
- [26] M. Y. Hémonnot, J. Reinhardt, O. Saldanha, J. Patommel, R. Graceffa, B. Weinhausen, M. Burghammer, C.G. Schroer, S. Köster, "X-rays reveal the internal structure of keratin bundles in whole cells," *ACS Nano* 10 (2016) 3553–3561.
- [27] D.J. Bray, T.R. Walsh, M.G. Noro, R. Notman, Complete structure of an epithelial keratin dimer: implications for intermediate filament assembly, *PLoS One* 10 (2015) e0132706.
- [28] S. Deb-Choudhury, J.E. Plowman, K. Rao, E. Lee, C. van Koten, S. Clerens, J.M. Dyer, D.P. Harland, "Mapping the accessibility of the disulfide crosslink network in the wool fiber cortex," *Proteins: Struct. Func. Bioinform.* 83 (2015) 224–234.
- [29] M. Feughelman, A model for the mechanical properties of the  $\alpha$ -keratin cortex, *Text. Res. J.* 64 (1994) 236–239.
- [30] M.A. Kasapi, J.M. Gosline, Micromechanics of the equine hoof wall: optimizing crack control and material stiffness through modulation of the properties of keratin, *J. Exp. Biol.* 202 (1999) 377–391.
- [31] D.S. Fudge, J.M. Gosline, "Molecular design of the  $\alpha$ -keratin composite: insights from a matrix-free model, hagfish slime threads," *Proc. R. Soc. London B: Biol. Sci.* 271 (2004) 291–299.
- [32] C.C. Pollitt, Anatomy and physiology of the inner hoof wall, *Clin. Techniques Equine Practice* 3 (2004) 3–21.
- [33] A. Lyne, D. Hollis, Development of horns in merino sheep, *Aust. J. Zool.* 21 (1973) 153–169.
- [34] C. Pollitt, The anatomy and physiology of the hoof wall, *Equine Veterinary Educ.* 10 (1998) 318–325.
- [35] M.W. Trim, M.F. Horstemeyer, H. Rhee, H. El Kadiri, L.N. Williams, J. Liao, K.B. Walters, J. McKittrick, S.J. Park, The effects of water and microstructure on the mechanical properties of bighorn sheep (*ovis canadensis*) horn keratin, *Acta Biomater.* 7 (2011) 1228–1240.
- [36] M.A. Kasapi, J.M. Gosline, Design complexity and fracture control in the equine hoof wall, *J. Exp. Biol.* 200 (1997) 1639–1659.
- [37] J.E.A. Bertram, J.M. Gosline, Fracture-toughness design in horse hoof keratin, *J. Exp. Biol.* 125 (1986) 29–47.
- [38] J. Douglas, C. Mittal, J. Thomason, J. Jofriet, The modulus of elasticity of equine hoof wall: implications for the mechanical function of the hoof, *J. Exp. Biol.* 199 (1996) 1829–1836.
- [39] J.E.A. Bertram, J.M. Gosline, Functional design of horse hoof keratin – the modulation of mechanical-properties through hydration effects, *J. Exp. Biol.* 130 (1987) 121–136.
- [40] M.A. Kasapi, J.M. Gosline, Strain-rate-dependent mechanical properties of the equine hoof wall, *J. Exp. Biol.* 199 (1996) 1133–1146.
- [41] D.M. Ebenstein, L.A. Pruitt, Nanoindentation of biological materials, *Nano Today* 1 (2006) 26–33.
- [42] I. Zlotnikov, E. Zolotoyabko, P. Fratzl, Nano-scale modulus mapping of biological composite materials: theory and practice, *Prog. Mater. Sci.* 87 (2017) 292–320.
- [43] Z. Liu, D. Jiao, Z. Weng, Z. Zhang, Water-assisted self-healing and property recovery in a natural dermal armor of pangolin scales, *J. Mech. Behav. Biomed. Mater.* 56 (2016) 14–22.
- [44] Y. Zhang, W. Huang, C. Hayashi, J. Gatesy, J. McKittrick, Microstructure and mechanical properties of different keratinous horns, *J. R. Soc. Interface* 15 (2018) 20180093.
- [45] K. Kareh, P. Lee, R. Atwood, T. Connolley, C. Gourlay, Revealing the micromechanisms behind semi-solid metal deformation with time-resolved x-ray tomography, *Nat. Commun.* 5 (2014) 4464.
- [46] Y. Wang, T.L. Burnett, Y. Chai, C. Soutis, P.J. Hogg, P.J. Withers, X-ray computed tomography study of kink bands in unidirectional composites, *Compos. Struct.* 160 (2017) 917–924.
- [47] D. Liu, B. Gludovatz, H.S. Barnard, M. Kuball, R.O. Ritchie, Damage tolerance of nuclear graphite at elevated temperatures, *Nat. Commun.* 8 (2017) 15942.
- [48] C. Popescu, H. Höcker, Hair – the most sophisticated biological composite material, *Chem. Soc. Rev.* 36 (2007) 1282–1291.
- [49] T. Bornschlög, L. Bildstein, S. Thibaut, R. Santoprete, F. Fiat, G.S. Luengo, J. Doucet, B.A. Bernard, N. Baghdadii, Keratin network modifications lead to the mechanical stiffening of the hair follicle fiber, *Proc. Natl. Acad. Sci.* 113 (2016) 5940–5945.
- [50] K. Johnson, M. Trim, D. Francis, W. Whittington, J. Miller, C. Bennett, M. Horstemeyer, Moisture, anisotropy, stress state, and strain rate effects on bighorn sheep horn keratin mechanical properties, *Acta Biomater.* 48 (2017) 300–308.
- [51] G. Rogers, Electron microscope studies of hair and wool, *Ann. N. Y. Acad. Sci.* 83 (1959) 378–399.
- [52] A.N. Parbhu, W.G. Bryson, R. Lal, Disulfide bonds in the outer layer of keratin fibers confer higher mechanical rigidity: correlative nano-indentation and elasticity measurement with an afm, *Biochemistry* 38 (1999) 11755–11761.
- [53] C.-C. Chou, E. Lepore, P. Antonaci, N. Pugno, M.J. Buehler, Mechanics of trichocyte alpha-keratin fibers: experiment, theory, and simulation, *J. Mater. Res.* 30 (2015) 26–35.
- [54] J. Reilly, D. Cottrell, R. Martin, D. Cuddeford, Tubule density in equine hoof horn, *Biomimetics* 4 (1996) 23–36.
- [55] A. Kitchener, J.F. Vincent, Composite theory and the effect of water on the stiffness of horn keratin, *J. Mater. Sci.* 22 (1987) 1385–1389.
- [56] M. Feughelman, A two-phase structure for keratin fibers, *Text. Res. J.* 29 (1959) 223–228.
- [57] E.H. Mojumdar, Q.D. Pham, D. Topgaard, E. Sparr, Skin hydration: Interplay between molecular dynamics, structure and water uptake in the stratum corneum, *Sci. Rep.* 7 (2017) 15712.
- [58] D. Labonte, A.-K. Lenz, M.L. Oyen, On the relationship between indentation hardness and modulus, and the damage resistance of biological materials, *Acta Biomater.* 57 (2017) 373–383.
- [59] L.J. Gibson, M.F. Ashby, *Cellular Solids: Structure and Properties*, Cambridge University Press, 1999.
- [60] L.J. Gibson, Biomechanics of cellular solids, *J. Biomech.* 38 (2005) 377–399.
- [61] J. Fang, G. Sun, N. Qiu, N.H. Kim, Q. Li, On design optimization for structural crashworthiness and its state of the art, *Struct. Multidiscip. Optim.* 55 (2017) 1091–1119.